

The ionization structure of multiple shell planetary nebulae

I. NGC 2438 [★]

S. Öttl¹, S. Kimeswenger^{2,1}, and A. A. Zijlstra³

¹ Institute for Astro and Particle Physics, Leopold Franzens Universität Innsbruck, Technikerstrasse 25, A-6020 Innsbruck, Austria
e-mail: Silvia.Oettl@uibk.ac.at

² Instituto de Astronomía, Universidad Católica del Norte, Avenida Angamos 0610, Antofagasta, Chile
e-mail: Stefan.Kimeswenger@gmail.com

³ Jodrell Bank Centre for Astrophysics, School of Physics and Astronomy, University of Manchester, Manchester M13 9PL, UK
e-mail: a.zijlstra@manchester.ac.uk

Received December 06, 2013; accepted xxxx nn, 2014

ABSTRACT

Context. In recent times an increasing number of extended haloes and multiple shells around planetary nebulae have been discovered. These faint extensions to the main nebula trace the mass-loss history of the star, modified by the subsequent evolution of the nebula. Integrated models predict that some haloes may be recombining, and not in ionization equilibrium. But parameters such as the ionization state and thus the contiguous excitation process are not well known. The haloes are very extended, but faint in surface brightness - 10^3 times below the main nebula. The observational limits lead to the need of an extremely well studied main nebula, to model the processes in the shells and haloes of one object. NGC 2438 is a perfect candidate to explore the physical characteristics of the halo.

Aims. The aim is to derive a complete data set of the main nebula. This allows us to derive the physical conditions, such as temperature, density and ionization, and clumping, from photoionization models. These models are used to derive whether the halo is in ionization equilibrium.

Methods. Long-slit spectroscopic data at various positions in the nebula were obtained at the ESO 3.6 m and the SAAO 1.9 m telescope. These data are supplemented by imaging data from the HST archive and from the ESO 3.6 m telescope, and archival VLA observations. The use of diagnostic diagrams draws limits for physical properties in the models. The photoionization code CLOUDY is used to model the nebular properties, and to derive a more accurate distance and ionized mass.

Results. We derive an accurate extinction $E_{B-V} = 0.16$, and distance of 1.9 ± 0.2 kpc. This puts the nebula behind the nearby open cluster M46 and rules out membership. The low-excitation species are found to be dominated by clumps. The emission line ratios show no evidence for shocks. The filling factor increases with radius in the nebula. The electron densities in the main nebula are $\sim 250 \text{ cm}^{-3}$, dropping to $\sim 10\text{--}30$ in the shell. We find the shell in ionization equilibrium: a significant amount of UV radiation infiltrates the inner nebula. Thus the shell still seems to be ionized. The spatially resolved CLOUDY model supports the hypothesis that photoionization is the dominant process in this nebula, far out into the shell. Previous models predicted that the shell would be recombining, but this is not confirmed by the data. We note that these models used a smaller distance, and therefore different input parameters, than derived by us.

Key words. (ISM:) planetary nebulae: general - (ISM:) planetary nebulae: individual: NGC 2438 - Stars: AGB and post-AGB

1. Introduction

Multiple shell planetary nebulae (MSPNe):

Planetary nebulae (PNe) are the ionized ejecta from an asymptotic giant branch (AGB) star. They are a short-lived phenomenon compared to a typical stellar lifetime, and are visible while the now post-AGB star crosses the Hertzsprung-Russell diagram (HRD) towards high temperatures, before entering the white-dwarf cooling track. Most of the luminous material originates from the stellar wind during the last thermal pulses on the AGB.

This paper deals with the physical conditions of a special type of PNe: Multiple-shell planetary nebulae (MSPNe), which are surrounded by faint outer shells and/or haloes. In recent times, an increasing number of haloes and multiple shells around PNe have been discovered. Although MSPNe are a familiar phenomenon, most of them are poorly studied and understood.

Previous research (e.g., Corradi et al. 2003, Zhang et al. 2012 or Ramos-Larios et al. 2012a&2012b) identified the existence as common feature for nearly-round nebulae. They appear during the evolution around the knee in the HRD and in the early part of the cooling track. The observed MSPN structures are the intricate result of the interaction of hydrodynamic and radiative processes, both during the AGB and the post-AGB phases. A detailed description of the mass loss history and the connection between the stellar winds and the huge extended circumstellar envelopes can be found in, e.g., Blöcker (1995) and Decin (2012). Due to the faintness of the haloes, up to a factor of 10^3 below the main nebula in surface brightness, most of them were discovered much later than the nebula itself.

Corradi et al. (2000), Schönberner & Steffen (2002) and Perinotto et al. (2004) used 1D radiative transfer hydrodynamic (RTH) models to calculate the evolution of this kind of nebulae. They modeled the full evolution of the PN starting at the AGB in a sophisticated way. These important models provide a

[★] Based on observations at ESO and SAAO, and HST archival data

very good representation of the surface brightness of MSPNe at an age of about 10 000 years. The RTH models result in outgoing shock fronts. At an age of about 10 000 years (assuming the Blöcker (1995) track of an $0.605 M_{\odot}$ central star), the resulting density profile peaks at $n_{\text{H}} \gtrsim 500 \text{ cm}^{-3}$ (and thus $n_{\text{e}} \gtrsim 560 \text{ cm}^{-3}$). The central star of the PN (CSPN) has a luminosity of $\approx 250 L_{\odot}$ and a temperature of $T_{\text{CSPN}} \approx 120 \text{ kK}$. In those models, the outer limit of the bright nebula is the limit of the hard UV radiation – a *radiation bounded* optically thick PN. The shell material is nearly recombined ($n_{\text{e}} : n_{\text{H}} = 1 : 10$), with a temperature of 2 000 K. Thus the $[\text{O I}] \lambda 6300 \text{ \AA}$ line is predicted to be about 6 times stronger than $\text{H}\beta$.

These kind of models are enormously important for the general understanding of the evolution. The layered structure predicted by the models compares well with observations. In this paper, we will investigate the ionization structure of a MSPN, in order to provide further observational constraints for the models.

In this work we use the nomenclature introduced by Chu et al. (1987) and Balick et al. (1992), but fully defined by Corradi et al. (2003), based on the evolutionary RTH models:

- the main nebula - also called 'rim' by them;
- the first thin surrounding structure including its outer weak intensity enhancement is called 'shell';
- the faint outer structures are called 'halo1' and 'halo2'.

NGC 2438:

Our target is a classical MSPN, used as 'benchmark' for the modeling (Corradi et al. 2000). NGC 2438 shows a bright inner main nebula; the geometry of the nebula is near round and closed. The diameter of the main nebula is about $60''$. The nebula indicates two slightly detached shells and a very faint halo (Fig. 1). This faint halo is most visible in the western part of the nebula and seems to have a circular shape. We can find ray-like structures and clumps in the nebula as well. The CSPN is not the bright star near the center, but the fainter one at the center of the nebula.

The only observational study of the nebula over a wide optical wavelength range and through the whole main nebula was obtained by Guerrero & Manchado (1999), with a single exposure at the ESO 1.5m telescope. They centered the slit on the brightest star near the center (not the CSPN), and integrated over wide areas along the slit. Guerrero & Manchado (1999) report no detection of the $[\text{O I}]$ line. This might be due to the strength of the telluric airglow line at this position. Further studies of the innermost regions around the CSPN were given by Torres-Peimbert & Peimbert (1977), Kaler (1983), Kingsburgh & Barlow (1994) and Kaler et al. (1990). All of them were focusing on abundances and they find a mild helium and nitrogen overabundance. The spectral investigation of Corradi et al. (2000) covered the regions of $[\text{O III}] \lambda 5007 \text{ \AA}$ and $\text{H}\alpha + [\text{N II}] \lambda 6548 \text{ \AA} + \lambda 6584 \text{ \AA}$ with a high resolution of $n70\,000$. They provide good results for the expansion of the nebula.

The CSPN was investigated in detail by Rauch et al. (1999), using non-local thermodynamic equilibrium (NLTE) stellar atmosphere models. The results are $\log(g[\text{cgs}]) = 6.62 \pm 0.22$, $T_{\text{CSPN}} = 114 \pm 10 \text{ kK}$, $L_{\text{CSPN}} = 570 L_{\odot}$, and $M_{\text{CSPN}} = 0.56 \pm 0.01 M_{\odot}$. The helium overabundance of the CSPN is slightly above the one found in the studies of the inner nebula mentioned before. Rauch et al. (1999) report that the nebula luminosity is an order of magnitude above the luminosity of the CSPN. We later show (see Sec. 4), that this discrepancy was not caused by the model, but by the photometry from literature they used. The low CSPN mass would imply a slow post-AGB evolution.

Based on the line ratios of $[\text{O III}] : \text{He II} : \text{H I}$ in the main nebula and the line ratio of $[\text{O III}] : \text{H I}$ in the shell, photoionization studies (Armsdorfer et al. 2002, 2003) state that the shell consists of ionized material. The required amount of ionizing UV photons can be obtained by a clumpy structure of the main nebula, allowing UV photons to escape. Such structures are established for some well-studied PNe, e.g., the Helix Nebula (O'Dell et al. 2005; Matsuura et al. 2009) or the Ring Nebula (Speck et al. 2003; O'Dell et al. 2003). In Dalnódar & Kimeswenger (2011), the positions of the spokes of enhanced intensity in the shell of NGC 2438 was shown to be correlated to holes in the main nebula. This supports the concept of a *matter bounded* structure. Recent studies of the MSPN IC 418 (Ramos-Larios et al. 2012a) and NGC 6369 (Ramos-Larios et al. 2012b) reveal very similar results: '*Radial filaments emanate outwards from most of the [N II] knots*'.

In this work we compiled own spectroscopy and multi-wavelength imaging data sets. Combining more information and data gives us the opportunity to search for the origin of the reported discrepancies and to draw detailed constraints for multi-dimensional RTH studies of MSPNe. We analyze long slit spectra, narrow-band images, a VLA radio map and HST archival data. We investigate the main nebula and the shell by means of a sophisticated spatially resolved CLOUDY model (Ferland et al. 1998, 2013).

2. Observations and data reduction

2.1. Spectroscopy

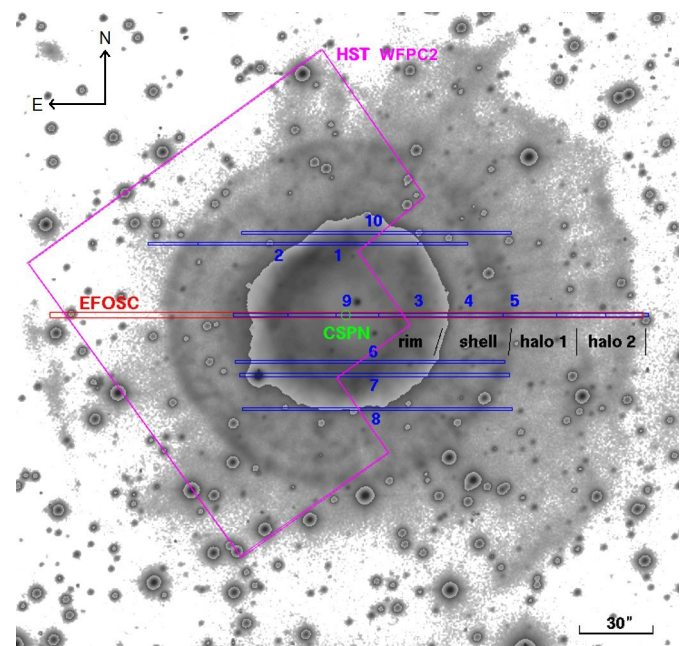


Fig. 1. An overview of the target observations. The background image is a $\text{H}\alpha$ EFOSC1 image. The spectrograph slits were all positioned in the E-W direction. The SAAO slits numbers correspond to those in Tab. 1. The CSPN and the region names as defined in Sec. 1 are shown and the field of view of the HST WFPC2 images is indicated as well.

Two independent spectroscopic data sets of NGC 2438 were used. The first spectroscopic data set was taken at the European

Southern Observatory (ESO) at La Silla in Chile. Observations during three nights in 1996 were obtained, using the 3.6 m telescope and the ESO Faint Object Spectrograph and Camera (EFOSC1¹) in long slit mode. The slit was positioned across the CSPN. These observations are summarized in Tab.1.

The second spectroscopic data set was taken 2002 at the South African Astronomical Observatory (SAAO) 1.9 m Radcliffe Telescope in Sutherland. The observations were obtained during four nights. Due to the short slit, several positions were taken - scanning the whole nebula. These observations are summarized in Tab. 1. The slit positions are indicated in Fig. 1.

All instrumental parameters of both observations and all the technical details are summarized in Tab. 2.

Table 1. The spectroscopic data set.

Nr.	Position		Date UT	airm.	expo. [sec]
	RA	DEC			
<i>ESO data</i>					
	7 ^h 41 ^m 50 ^s .51	-14°44'07".7	02-11 02:52	1.034	3600
	7 41 50.51	-14 44 07.7	02-13 01:18	1.119	3600
<i>SAAO data</i>					
1a	7 ^h 41 ^m 50 ^s .88	-14°43'38".5	04-16 17:31	1.01	1800
1b	7 41 50.87	-14 43 38.5	04-16 18:04	1.07	600
2	7 41 52.22	-14 43 38.5	04-16 18:19	1.08	1800
3	7 41 48.44	-14 44 07.7	04-17 17:21	1.01	1800
4	7 41 47.13	-14 44 07.7	04-17 18:18	1.08	1800
5	7 41 45.96	-14 44 07.7	04-17 18:53	1.08	1800
6	7 41 49.85	-14 44 27.0	04-18 17:43	1.01	1800
7	7 41 49.73	-14 44 32.3	04-18 18:19	1.08	1800
8	7 41 49.67	-14 44 46.3	04-18 18:52	1.25	1800
9	7 41 49.91	-14 44 07.7	04-19 17:38	1.03	1800
10	7 41 49.68	-14 43 34.0	04-19 18:42	1.12	3600

Notes. In the ESO observations, the slit was centered and guided at the CSPN. In the SAAO observations, the slit was moved to various positions in the target, indicated by the numbers. The coordinates were calibrated later using 2MASS stars. The airmass in both observations is given at mean time of the observation.

Table 2. Technical details and instrumental parameters.

Observatory	ESO	SAAO
CCD	# 26 Textronic	SiTe
pixel size	571 × 520	266 × 1798
grism/grating	# 10 - 150 lines/mm	# 7 - 300 lines/mm
slit width	1"	1"
slit length	243"	110"
direction	E-W fixed	E-W
spatial separation	0'.64 per pixel	0'.73 per pixel
wavelength range	λ3780Å to λ5508Å	λ3700Å to λ7400Å
sampling	3.0 Å per pixel	2.3 Å per pixel
resolution	6.0 Å	4.5 Å

Notes. The spatial separation is along the slit. The blaze wavelength for the SAAO grating # 7 is 4600Å.

The spectra were reduced by standard MIDAS (Warmels 1991) routines. Careful corrections for variations of the slit width along the slit were applied by adding the flatfield images.

¹ www.eso.org/sci/facilities/lasilla/instruments/efosc/History.html

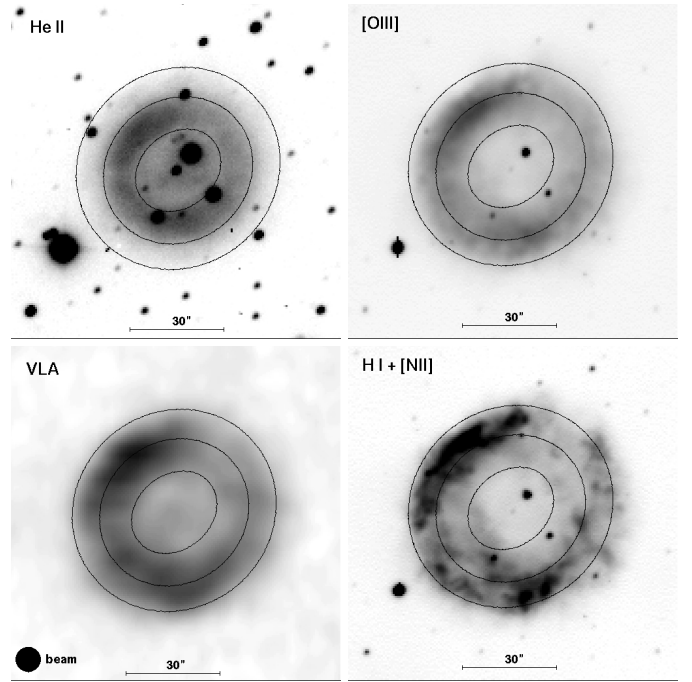


Fig. 2. The direct images of the main nebula. First row: He II ($\lambda 4686\text{\AA}$) & [O III] ($\lambda 5007\text{\AA}$); second row: VLA (20 cm) & H I ($\lambda 6563\text{\AA}$) + [N II] ($\lambda 6548\text{\AA}$ + $\lambda 6584\text{\AA}$) (same orientation as shown in Fig. 1 - N is up, E is left). The ellipses are derived from the images of the He II line. While the He II emission is concentrated clearly towards the inner edge of the main nebula, the [O III] and VLA images have about the same appearance.

The variations were about 2% in the EFOSC1 spectra and up to 17% in the SAAO spectra. The variations show no dependency on wavelength. As the outer haloes are not visible east of the nebula in the ESO data, the night sky could be taken directly from the slit positions outside the nebula and the shell. Additionally, the sky for the SAAO data could be taken from data from other, smaller nebulae, which were observed by Thomas Rauch during the same nights. These other PNe without halo were used to estimate straylight contamination of the surroundings. Both instruments do not show any contamination down to the noise level of the images. For the extraction of the nebular lines and proper suppression of local free-free continuum, the nearest empty region along the slit was used. Usually, the nearest region was directly redwards and bluewards of each line. In some cases only one side was used, to avoid blending with other lines. To improve S/N, the width of the region was 3 times the FWHM of the lines. The contribution was found to be fairly small within the main nebula. Only at the very blue end the readout noise was detected a few times. Outside the main nebula, towards shell and halo, no variation above the sky level within the limits of the readout noise was detected.

Corrections of differential refraction were applied on both data sets, using the algorithm of Fluks & The (1992). These corrections were applied to the standard stars as well as to the CSPN spectra, to obtain the absolute flux calibrations. Due to the observations near zenith, the corrections for the nebula are very small and the effect of variation of the parallactic angle during the long nebula exposures are negligible. In case of the standard stars, we have exposures of 1 and 5 minutes only, during which the paral-

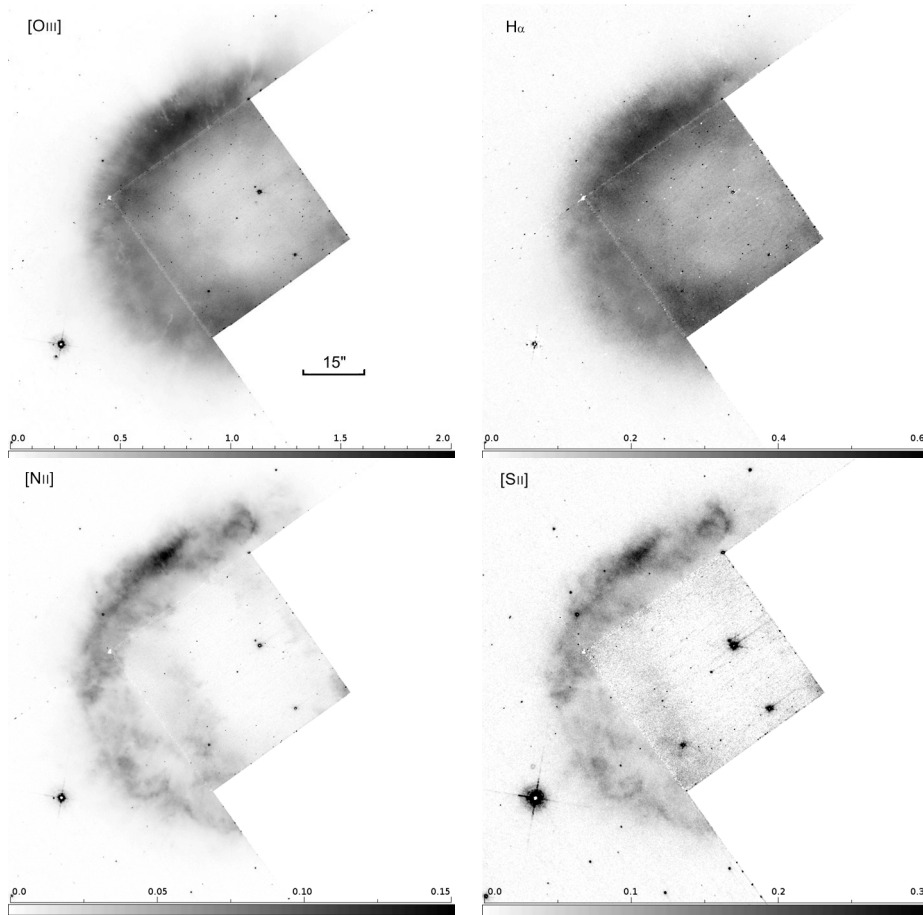


Fig. 3. The HST images of the main nebula. First row: [O III]($\lambda 5007\text{\AA}$) and $H\alpha$ after subtracting [N II] contribution (see text); second row: [N II] ($\lambda 6584\text{\AA}$) and [S II]($\lambda 6716\text{\AA} + \lambda 6732\text{\AA}$). The images are in the same orientation as shown in Fig. 1 and cover the field of view shown there. The similarities in the structures are obvious.

lactic angle was constant. The differential refraction correction is up to 9% at the blue end of the spectra.

After applying all corrections from night to night, the flux differences of the standard stars were only a few percent. For overlapping observations between the SAAO and the ESO spectra, a variation below 5% of the bright lines (e.g., [O III]) was found. For the fainter lines (e.g., Ar II, $H\delta$, ...), a typical variation of less than 10% was found. Taking conservative estimates of systematic effects, we assume the overall absolute flux accuracy to be better than 12% in the main nebula, and better than 20% in the shell. Differential values (e.g., line ratios) are expected to be better than 5%.

2.2. Imaging

Direct images using narrow-band filter [O III] $\lambda 5007\text{\AA}$ (ESO filter #686), He II $\lambda 4686\text{\AA}$ (ESO filter #512) and $H\alpha + [\text{N II}]$ $\lambda 6548\text{\AA} / \lambda 6584\text{\AA}$ (ESO filter #691) were obtained at the ESO 3.6 m telescope. The absolute flux calibration was scaled from the long slit spectra. The $H\alpha$ filter #691 contains significant contributions of both [N II] lines. The filter response was used to derive a sensitivity of 95% of the $\lambda 6548\text{\AA}$ line and 75% of the $\lambda 6583\text{\AA}$ line (relative to peak transmission).

As a byproduct of an investigation of the nearby bipolar nebula OH 231.8+4.2 (Taylor & Morris 1993), VLA radio observations of NGC 2438 were obtained and made available to us by the authors.

The morphologies in the different images show variations (Fig. 2). In the [O III] image and in the VLA image, the same nebula structures, elongation, and central cavity were found. The

He II image shows more concentration towards the inner region. Despite the Bowen fluorescence, the decoupling of the helium image and the oxygen image shows the limit of the optically thick region in the helium Lyman continuum, used in the modeling part (Sec. 6). The ($H\alpha + [\text{N II}]$) image is dominated by substructures and clumps. The rim of the main nebula is slightly elongated by about 0.9 : 1 (Fig. 2). The ellipticity is fairly small (0.84, 0.91 and 0.94 from inner to outer ellipse) and the position angles are constant.

Additionally, a data set of NGC 2438 in the HST archive was retrieved. The images, taken in September 2008, do not cover the whole nebula. The data set is summarized in Tab. 3. The inner region was covered by the high resolution PC camera and has a very low signal to noise ratio. The images are not deep enough to show structures of the shell or the haloes (Fig. 3). They were used to analyze shock signatures (see Sec. 5.3).

Table 3. Observation log of the HST archival images (all taken with WFPC2).

line	filter	exposure time time [s]	observing date&time
$H\alpha + [\text{N II}]$	F656N	1000	2008-09-19 09:51:17
[O III]	F502N	1000	2008-09-19 11:25:17
[N II]	F658N	500	2008-09-19 13:01:17
[S II]	F673N	400	2008-09-19 13:13:17

The post-flight measurements of the WFPC2 filters, the expansion velocity and the systematic velocity, measured by Meatheringham et al. (1988) and by Corradi et al. (2000),

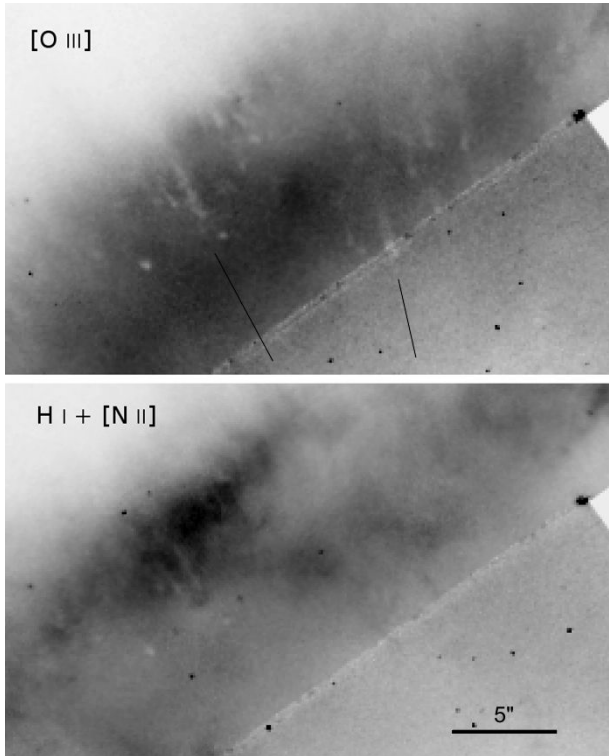


Fig. 4. A zoom of the N-E region of the main nebula from the HST images. The cometary knots are especially pronounced in the [O III] images. The shadows point exactly away from the CSPN (direction indicated by two lines).

were used to calculate the effect of the line width on the filter transmission. We obtained a contamination by [N II] λ 6548, and [N II] λ 6584 in the F656N filter band of 39% and 2%, respectively. In contrast, the F658N filter has a sensitivity of just about 1.7% for H α . Both filters have the same peak transmission. Thus we were able to directly obtain a pure H α image, using the image of F658N and the known line ratio of [N II] λ 6548 / [N II] λ 6584. This H α image shows exactly the same morphology as the [O III] image and VLA image shown before. The [N II] image and the [S II] image indicate identical structures throughout all regions of the nebula. Additionally, the [O III] and the H α images show some cometary knots and ray-like structures pointing outwards the edges (Fig. 4). The shadow tails of the knots, pointing exactly away from the CSPN as result of the shielding of hard UV, are clearly visible only in [O III]. The radiation to ionize the H I is provided by the diffuse nebula radiation, thus no shadows are formed in H α .

3. Extinction and CSPN parameters

The foreground extinction towards the nebula was derived using the Balmer line series in the SAAO spectra. The intrinsic line intensities R_{intr} for the case B recombination calculated by CLOUDY and the interstellar extinction curve from Osterbrock & Ferland (2006) of the four isolated Balmer lines from λ 4102Å to λ 6563Å were used to derive the interstellar foreground extinction from the measured line ratios R by:

$$E_{B-V} = a \times \log\left(\frac{R}{R_{\text{intr}}}\right) = 0^m16 \pm 0^m01 .$$

The intrinsic line ratios R_{intr} were determined iteratively, starting with $T_e = 10\text{kK}$, taken from the table in Osterbrock & Ferland

(2006), and calculated with CLOUDY using the temperature derived from the N II lines (see Sec. 6, Tab. 6). The final CLOUDY model gives additional information about the blended He II lines. The flux contribution at these temperatures is 1-3% only. Thus the error introduced for line ratios by neglecting the contribution of the He II lines should be in the order of 1% only. As shown in Tab.4, all line ratios lead to the same extinction. Thus the assumptions of case B recombination and standard extinction apply very well. The spread is remarkably small.

Table 4. Extinction measurement with the Balmer lines.

line	R	R_{intr}	a	E_{B-V}
H α /H β	3.300	2.790	2.21	0.1613
H γ /H β	0.443	0.476	-0.517	0.1599
H δ /H β	0.236	0.262	-3.52	0.1612

To search for intrinsic extinction in the nebula, the spatial distribution of the ratio R was investigated. We used H α from the SAAO data, and H β from the ESO data, as they are deeper in the outer shell (Fig. 5). The results show no correlation in the position and the line intensity. Even in the thin shell the same ratio was found.

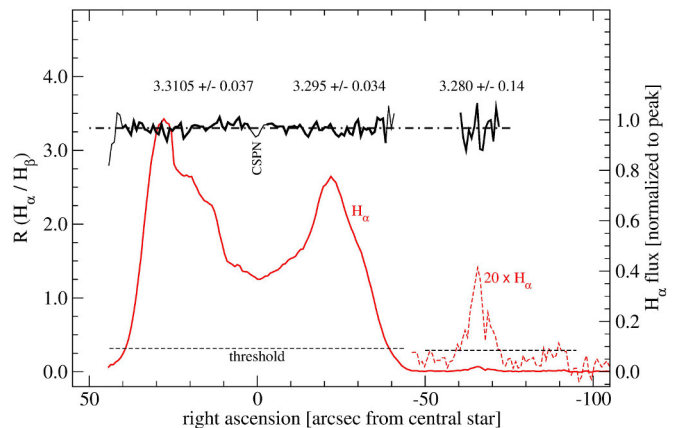


Fig. 5. The spatial distribution of the line ratio $R = \text{H}\alpha/\text{H}\beta$ to search for intrinsic extinction. To cover homogeneous S/N ratios, a threshold of $3.5 \times$ below the S/N peak was chosen. Also the region around the CSPN was excluded. For the shell, the same procedure was applied, but $20 \times$ fainter.

Guerrero & Manchado (1999) derive an extinction of $E_{B-V} = 0^m12 \pm 0^m03$. They note that their solution of the series does not fulfill the theoretically expected values for such plasmas after de-reddening. To obtain a reasonable signal to noise (S/N) ratio, they integrate over large regions along the slit. The off-centered slit leads to non-radial terms in the integrated line intensities. Taking into account the offset of their slit, we find a fair agreement at the blue end.

A spectroscopic comparison of the hot white dwarf (WD) standard star EG 274 and the CSPN leads to an independent test of the calibration. The CSPN was completely covered by the ESO spectra and by three spectra (3, 4 and 9) in the SAAO data set. The combined information from three different nights and two different instruments reduces the calibration errors and excludes systematic effects in the data reduction. The de-reddened SAAO spectrum, overlaid with the WD spectrum of the stan-

standard star EG 274, shows the high accuracy of the extinction value and of the calibration over the whole wavelength range (Fig. 6). Thus we were able to use this to secure the photometry. The CSPN flux at $\lambda 5500\text{\AA}$ is $2.3 \times 10^{-13} \text{ erg cm}^{-2} \text{ s}^{-1} \text{ \AA}^{-1}$ with an *rms* of 5%. Using the zero point by Colina et al. (1996), we obtained values of $V = 16^m 82 \pm 0^m 09$, and $V_0 = 16^m 32 \pm 0^m 10$ for the CSPN.

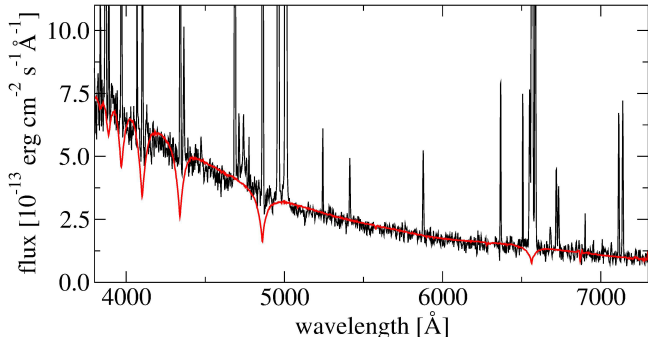


Fig. 6. The CSPN (thin black line), without removing the nebula emission lines, and the standard star EG 274 overlaid (smooth red line - scaled and the extinction $E_{B-V} = 0^m 16$ applied).

4. Distance determination

There are several distance estimates of NGC 2438 in the literature, leading to values between 0.8 and 4.3 kpc.

Rauch et al. (1999) use the spectroscopy of the central star to derive temperature and surface gravity. They use $V = 18^m 0$, from Acker et al. (1992), and a reddening in the range of $0^m 0 < E_{B-V} < 0^m 34$. This leads to a large distance of 4.3 kpc and large errors. Using the CSPN parameters and the extinction derived in this work (see Sec. 3), we obtained a new spectroscopic distance of $2.0^{+0.4}_{-0.35}$ kpc with their model.

For the open cluster M 46 at the same line of sight, a distance of 1.51 kpc (Sharma et al. 2006) is given from optical CCD photometry with $E_{B-V} = 0^m 10 \pm 0^m 02$. Using infrared 2MASS data leads to an extinction of $E_{B-V} = 0^m 13$ and a distance of 1.7 ± 0.25 kpc (Majaess et al. 2007). The abundance of $[\text{Fe}/\text{H}] = -0.03$ (Paunzen et al. 2010) is very near to solar and the cluster is very rich. The fits of the evolutionary tracks and thus the distances and extinction values are reliable. Our extinction value places the PN behind the cluster. This result agrees with Kiss et al. (2008), who already rule out a cluster membership of the PN due to a large discrepancy in the radial velocity.

Radio observations yield distance estimators based on a number of distance scales with different assumptions and calibration. Using the high resolution VLA radio map of Taylor & Morris (1993), we got a radio flux of 74.9 ± 1.6 mJy at a frequency of 1.5 GHz (20 cm). This is slightly lower than the result of 80.3 ± 3.2 mJy, given in the NVSS (Condon et al. 1998). The difference is due to the fact, that the background source at $07^h 39^m 35^s 8s -14^\circ 28' 04''$ was not resolved by the survey. Using survey data from NVSS, PMN and F3R, the radio spectral energy distribution (SED) can be fit by a pure free-free radiation (Vollmer et al. 2010). Thus using $I = I_0 \nu^{-0.1}$ we derived a radio flux of $S_{6\text{cm}} = 66$ mJy. This corresponds well to the $S_{6\text{cm}} = 67$ mJy, given by Zijlstra et al. (1989) in their VLA survey. Using the calibration of van de Steene & Zijlstra (1995) of the radio continuum brightness temperature, we obtained a

Table 5. Dimensions of the nebula, derived for a distance of 1.9 kpc.

	measured diameter [$''$]	radius [$\times 10^{17}$ cm]	dynamic age [years]
central wind cavity	24	3.5	
main nebula	76	10.8	$12 \dots 17 \times 10^3$
shell	144	20.5	
first halo	189	27.	
second halo	246	35.	

Notes. The dynamical age agrees well with the 20 kyears derived as evolutionary age for the CSPN by Rauch et al. (1999).

distance of 1.8 ± 0.3 kpc. The scale by Bensby & Lundström (2001) results in 2.1 ± 0.3 kpc. The errors mainly originate in the way we determined the radius. We used the 20% contour level of the H I and the [O III] image, averaged over the ellipticity. The errors are estimates, varying inwards to the slightly smaller VLA image and outwards to the 5% level of the optical images. The statistical distance scale of Schneider & Buckley (1996) results in a lower distance of about 1.2 kpc. But such low distances tend to be excluded by the extinction derived for the nebula and for the open cluster M 46.

Considering the individual spectroscopic distance and the distance of M 46 as a foreground object, we adopt a distance of 1.9 ± 0.2 kpc for NGC 2438. The error estimate makes use of the fact that Majaess et al. (2007) and Paunzen et al. (2010) do not find intrinsic extinction variations in M 46, and thus NGC 2438 has to be beyond the cluster. This is consistent with the nebula distance scale by van de Steene & Zijlstra (1995) and Bensby & Lundström (2001). Other statistical distance scales, giving results around 1 kpc, have to be excluded due to the values found for the open cluster M 46. The resulting dimensions of the nebula are summarized in Tab. 5.

5. Spectral analysis

5.1. General appearance

The combined nebular spectra at the slit position through the CSPN are shown in Fig. 7. The spectra obtained at the other positions were compared to the combined spectra at the center, as a function of distance from the CSPN. The variations between different lines are slight. Only the clumpy low excitation species [N II] and [S II] vary up to a factor of 2 in their line ratios. This compares well with the results of the imaging and the radio observations (see Fig. 2). The profiles show three groups:

- The high excitation species (level > 30 eV or ionization > 60 eV) are concentrated to the center.
- The medium excitation species (level > 10 eV or ionization > 20 eV) are smoothly distributed over the whole nebula.
- The low excitation species (levels < 5 eV and single ionized or neutral) are dominated by clumps.

Only the triplet $\text{He I } \lambda 4472\text{\AA}$ line and the singlet $\text{He I } \lambda 6678\text{\AA}$ lines, due to the extreme long lifetime of the $\text{He I } ^3\text{S}$ (19.82 eV) state of the singlet, faking a kind of ground state, behave not straight forward to the criteria given above.

Although He II and [O III] are coupled via the Bowen fluorescence, the spatial profiles of these two elements differ. But within one group, the profiles are identical.

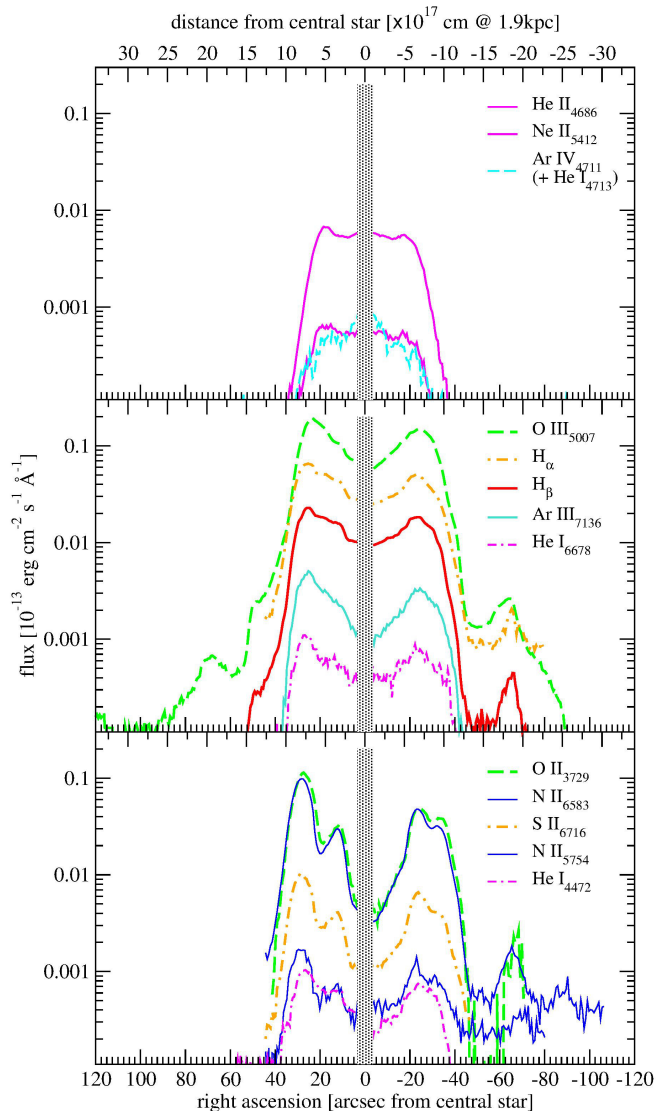


Fig. 7. Various lines of the nebula (logarithmic representation). The different spectral regions originate from different spectra (ESO & SAAO) and thus vary in S/N ratio at similar physical intensities. The panels show the excitation groups (criteria see text). The high excitation species (upper panel) concentrate to the central region. The medium excitation species (middle panel) are smoothly following the total brightness and the radial behaviour of the VLA image throughout the nebula. The low excitation species (lower panel) are dominated by clumpy structures. The O II $\lambda 3729$ is at the edge of the CCD and its flux calibration is very uncertain. It is added only for comparison of the profiles.

These groups and the behavior of the low excitation species are similar to those described by Ramos-Larios & Phillips (2012) for the PN NGC 2371. It also resembles the $H\alpha$: [N II] surface brightness profiles of NGC 6369 (Ramos-Larios et al. 2012b). The change of the excitation gives strong constraints for the optical thickness in the models (see Sect. 6).

5.2. Density distribution and electron temperature

The diagnostic density and temperature diagrams (described in Osterbrock & Ferland (2006) and Proxauf et al. (2014)) provide the input and boundary conditions. Despite the strong

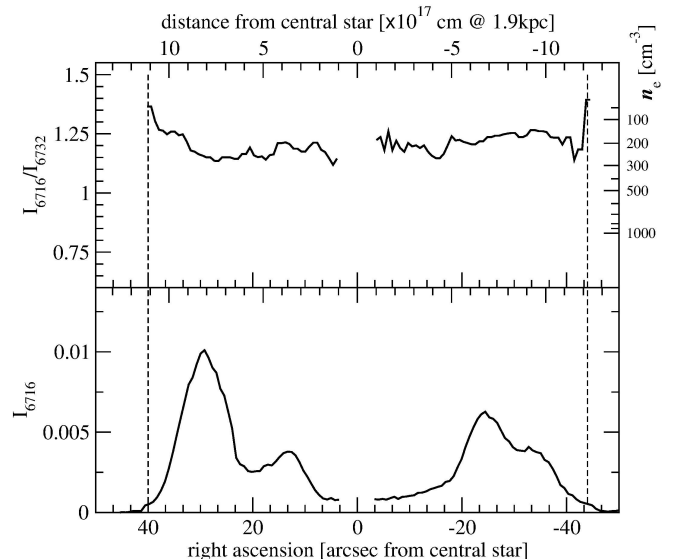


Fig. 8. The density derived from [S II], in E-W direction through the CSPN. The line ratio (upper panel) and the electron density is nearly constant. The density profile does not follow the strong surface brightness variations (lower panel).

variation in intensity, the density derived with [S II] results in a flat distribution (Fig. 8), with values of $200 \leq n_e \leq 300 \text{ cm}^{-3}$. This corresponds well to the value of 300 cm^{-3} , calculated by Meatheringham et al. (1988), using the O II $\lambda 3727\text{\AA}/\lambda 3729\text{\AA}$ doublet and integrating over the whole nebula. Both detections suffer from the fact that only low excitation species were used.

Near the peak intensity of the main nebula, we could even detect Cl III $\lambda 5517\text{\AA}/\lambda 5537\text{\AA}$. Throughout a large fraction of the whole nebula, we found Ar IV $\lambda 4711\text{\AA}/\lambda 4740\text{\AA}$. Both doublets reflect the density of the high excitation plasma. However, as shown in Stanghellini & Kaler (1989) and in Copetti & Writzl (2002), those lines are only suited for slightly higher densities. An upper limit of the density of 300 to 400 cm^{-3} is stated.

The [O III] ($\lambda 4958\text{\AA} + \lambda 5007\text{\AA}$)/ $\lambda 4363\text{\AA}$ ratios along the slit result in an electron temperature of 10 000 to 11 500 K in the main nebula. A rise in the shell is suggested (see Fig. 9). The transition to the shell is marked by dashed lines with $1/10$ and $1/100$ of the peak intensity. The result reaches up to 13 000 K, using the new calibration of Proxauf et al. (2014). Because of the weakness of the [O III] $\lambda 4363\text{\AA}$, which is about 100 times fainter compared to the [O III] $\lambda 5007\text{\AA}$ emission, this may be an overestimation. There is no indication for a significant decline in temperature, as it would be expected for a recombining halo. The presence of the $\lambda 4363$ line ($> 5eV$) confirms a high temperature. Only in the main nebula we are able to derive the [N II] ($\lambda 6548\text{\AA} + \lambda 6583\text{\AA}$)/ $\lambda 5755\text{\AA}$ line ratios. The results are very close to that of [O III] (see Tab. 6). This implies that we see the same material of the nebula in two different excitation states. A third temperature diagnostic is given by Keenan et al. (1988), using Ar III ($\lambda 7135\text{\AA} + \lambda 7751\text{\AA}$)/ $\lambda 5192\text{\AA}$. Unfortunately, our spectral resolution is insufficient to detect Ar III $\lambda 5192\text{\AA}$ in the blend with the N I $\lambda 5198\text{\AA} + \lambda 5200\text{\AA}$ lines.

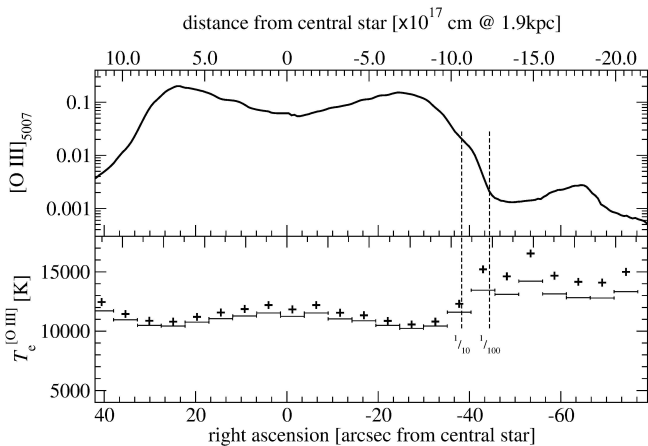


Fig. 9. The intensity (upper panel) of the $[\text{O III}] \lambda 5007 \text{ \AA}$, and the electron temperature using $[\text{O III}] (\lambda 4958 \text{ \AA} + \lambda 5007 \text{ \AA}) / \lambda 4363 \text{ \AA}$ ratios along the slit (lower panel). Logarithmic scale is used to show the shell and the even further extended halo. The flux scale is the same as in Fig. 7. The plus signs indicate the solution by exponential formula of Osterbrock & Ferland (2006). The bars give the solution using the new calibration of Proxauf et al. (2014).

5.3. Searching for shock signatures

As the radiative transfer hydrodynamic (RTH) models predict shocks during certain stages of the evolution (Corradi et al. 2000, Schönberner & Steffen 2002, Perinotto et al. 2004), we searched carefully for shock signatures, to exclude possible regions where the photoionization model does not work.

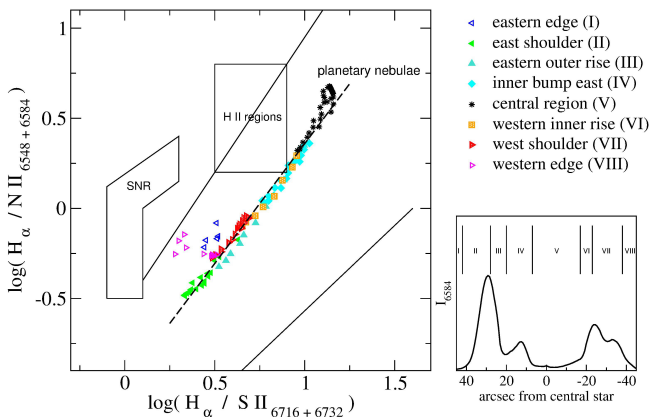


Fig. 10. The diagnostic diagram of the separation of shocked nebulae from photoionized PNe (after Magrini et al. 2003). The points follow the sequence of the ionization class towards the center. The dashed gives a fit through the good data points (filled symbols). No dependency on rise or fall of the intensity can be found (small panel).

Originally shown by García Lario et al. (1991), and later investigated more in detail by Magrini et al. (2003), the ratios of $\log(\text{H}\alpha/[\text{N II}])$ vs. $\log(\text{H}\alpha/[\text{S II}])$ can be used to separate photoionized PN plasma from shocked gas, as seen, e.g., in supernova remnants (SNRs). Schmeja & Kimeswenger (2001) have shown that, for photoionized gas of symbiotic Miras, the position in the diagram is an indicator for the level of excitation as

well. The spectra of the main nebula of NGC 2438 show the excitation tendency from inside to outside well (Fig. 10). There is no signature of a deviation from expected line ratios. This is an indication that photoionization is the dominating mechanism for the excitation of the material. The fit line, used for the further analysis, has an inclination of 1.33 and a constant of 0.73 along the abscissa. A few data points at the outermost edge suffer from weak sulphur lines. At least one order of magnitude deeper spectra would be required to extend this kind of analysis towards the shell. Although the HST images do not cover the whole nebula

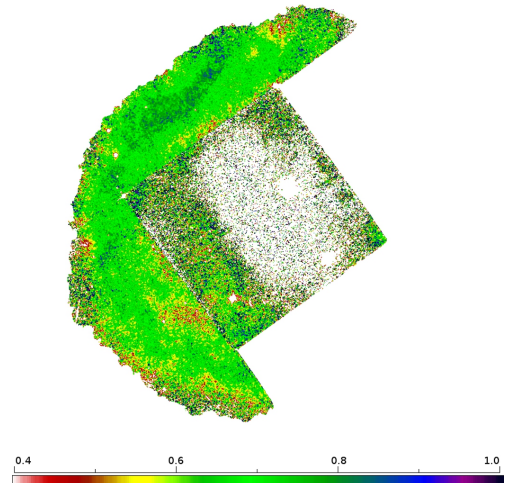


Fig. 11. The $\log(\text{H}\alpha/[\text{N II}]) - \log(\text{H}\alpha/[\text{N II}])$ image obtained from the HST frames. It is based on the same analysis as in Fig. 10. The expected value should be the same as the incline (0.7-0.8) of the trendline through the data points in Fig. 10.

and are very noisy (especially in $[\text{S II}]$ in the PC camera part), they were used to obtain a similar analysis. The linear fit in Fig. 10 has a slope of 1.33. The HST Filter F658N covers only the $[\text{N II}] \lambda 6584 \text{ \AA}$ line and the line ratio of $[\text{N II}] \lambda 6584 \text{ \AA}$ is known to be 1:3, so the factor goes to unity. As both $[\text{S II}]$ lines are covered by the HST filter, the abscissa stays untouched. The subtraction $\log(\text{H}\alpha/[\text{N II}]) - \log(\text{H}\alpha/[\text{S II}])$ thus should result in the constant along the abscissa, if the whole nebula follows the tendency given in the region covered by the spectra. Fig. 11 clearly shows this behavior. As outer boundary the level in the H I image at 2.5% of the peak intensity was chosen.

Recently, Guerrero et al. (2013) suggested to use the $[\text{O III}]/\text{H}\alpha$ ratio to unveil shocks in regions of higher temperature. In those regions, nitrogen and sulfur are at least double ionized, and thus, no strong $[\text{N II}]$ and $[\text{S II}]$ lines are expected. They show that shocks should indicate sudden changes of the line ratio. They use similar HST archive data, but excluded our target due to possible contamination in the F656N filter with nitrogen lines. As discussed in Sec 2.2, in this case the images taken with F658N can be used in order to correct for contamination. Fig. 12 shows the result for our target. The line ratio is fairly constant: no shock signatures could be found in this target in the region covered by the images.

6. Model and discussion

All calculations were performed with version C10 of CLOUDY (Ferland et al. 1998). After the release of version C13 (Ferland et al. 2013), the resulting models were recalculated with the new

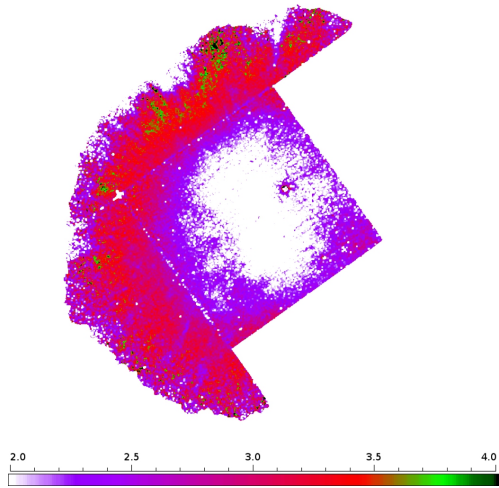


Fig. 12. The $[\text{O III}]/\text{H}\alpha$ image from the HST data. No sudden changes in the line ratio can be found.

version. No differences were identified between all results. The density profile was parameterized in 12 shells of 5×10^{16} cm. The nomenclature used here is the same as mentioned in Sect. 1.

6.1. The main nebula

In the main nebula, the strong variation of the $[\text{S II}]$ flux (see Fig. 8) and, on the other hand, the constant density given by the diagnostic diagrams require a change of the filling factor in the middle of the main nebula. This has been parameterized with two free parameters, giving the filling factors inside and outside a critical distance. The latter was identified by changes in the direct images. This is similar to the observed changes in clump frequencies in the Helix Nebula, which was recently discovered to be also a multiple-shell planetary nebula (MSPN) (Zhang et al. 2012). The optical images of the Helix Nebula do not cover all radii (O'Dell et al. 2005) and show a difference in number density at a line about 40% of the radius for the large knots. Matsuura et al. (2009) describe a low frequency of isolated H_2 clumps in the inner half of the nebula and a strong increase to a few hundred isolated knots per square arcminute in a region they call the inner ring (out to about 70% of the radius). After that region, a dense, cloudy structure abruptly starts, with almost no individual, isolated knots with tails, but with a nearly complete surface coverage. According to a comparison with a model originally computed for NGC 2436 (Vicini et al. 1999) by Speck et al. (2003), the Helix Nebula should be just on the edge to destroy the cold molecular knots, with its age of $19\,000^{+10\,000}_{-8\,000}$ years very similar to our target. In the Ring Nebula, Speck et al. (2003) and O'Dell et al. (2003) find similar overall behavior. But the Ring Nebula is assumed to be much younger ($5\,000^{+2\,500}_{-1\,700}$ years) and may still be evolving, and thus by a ploughing effect colliding smaller knots may combine to bigger ones or even more knots and clumps may be formed. Speck et al. (2003) also show, in their narrow band imaging, that the transition to the region with a high number density of no longer individual H_2 clouds is coincident with a sudden drop in the $\text{He II}/[\text{O III}]$ ratio. In our investigation, the sudden drop of the $\text{He II } \lambda 4686\text{\AA}$ demands such a change as well. The position of the change of the filling factor is thus fixed at 6×10^{17} cm.

An accurate model of the CSPN is essential for an appropriate modeling of the whole nebula. As shown by Armsdorfer

et al. (2002), the influence of the chosen CSPN model is crucial, in particular for the strength of the helium lines. Thus we used state-of-the-art H-Ni NLTE CSPN models provided by the Tübingen group (Rauch 2003, Ringat 2012). The stellar parameters given by Rauch et al. (1999) were used. The temperature was varied within one sigma of their original result. The spatial distribution of the line ratios, used for excitation and ionization as discussed in Mikołajewska et al. (1999), Phillips (2004) and Reid & Parker (2010), were used for an initial guess of the fitting procedure (see Fig. 13). The often used line ratios including $[\text{O II}]$ were not used here, as this $[\text{O II}]$ line is sensitive to density variations. Additionally, the line is just at the edge of the CCD chip and therefore less reliable.

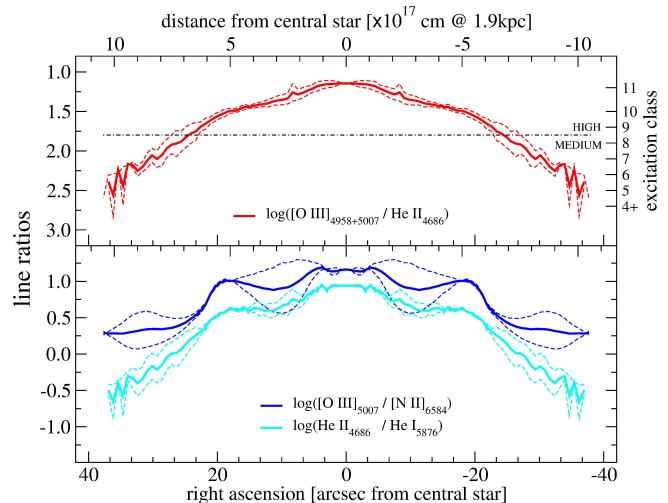


Fig. 13. The excitation and ionization sensitive line ratios. The dashed lines are the spectra along the slits through the center in original orientation (E-W) and the same spectrum reversed in direction to see the asymmetries. The thick lines are the average of both directions. The excitation class and the level of separation of medium to high excitation is used according to the calibration by Reid & Parker (2010).

Only the spatial profiles of $[\text{O III}] \lambda 5007\text{\AA}$, $\text{H}\alpha$, $\text{He I } \lambda 4471\text{\AA}$ and $\text{He II } \lambda 4686\text{\AA}$ were used to fit the free parameters of the nebula. For helium, the $\lambda 4471\text{\AA}$ line was used instead of the brighter $\lambda 5876\text{\AA}$ line, because it was covered by the significantly deeper ESO spectra. The fitting of the stellar temperature is completely dominated by the He I to He II line ratio. The He II to $[\text{O III}]$ ratio in the inner region can be described only with the CSPN model by Rauch et al. (1999). This suggests, that the inner region is dominated by the products of the stellar winds from the current photosphere of the CSPN. All other abundances were taken from the intrinsic set for PNe in CLOUDY by Aller & Czyzak (1983) and Khromov (1989). There were not enough lines to do detailed, spatially resolved abundances for other elements in this fitting procedure as free parameters. The best fit model is summarized in Tab. 6.

After fitting the whole set of free parameters, all other detected lines in the spectra are calculated (Fig. 14, Tab. A.1). There is no need for any iteration or feedback on the model. Even within the errors, no major deviations from the abundances seem to be required.

The simple model of the VLA data (see Fig. 14) was produced by using the free electrons of hydrogen and helium and assuming

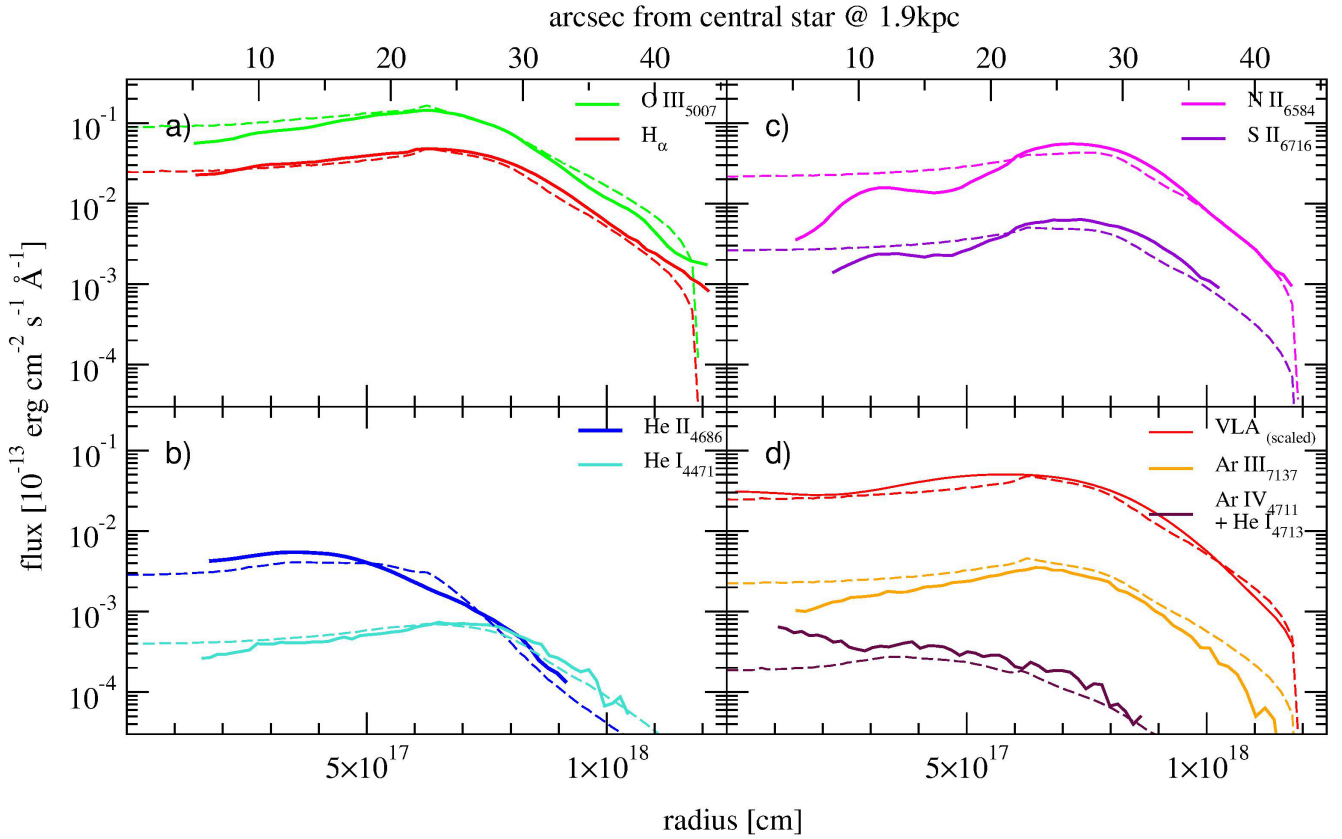


Fig. 14. The complete CLOUDY model of the main nebula. The dashed lines give the observational data, while the full lines are giving the model. The spectral lines in the left panels (a) and (b) are used to fit the free parameters of the density law, the filling factor and the temperature of the CSPN. The right panels (c) and (d) give the results derived for other lines from the best fit model. The VLA intensities were arbitrary scaled up to the same level as the peak in $H\alpha$.

only free-free radiation. The radio flux density was scaled to the same level of peak as the $H\alpha$ line, to fit into the scale of the plot. Additionally it is smeared with a gaussian, representing the beam size given by Taylor & Morris (1993). Also shown in Fig. 14, the feature around $\lambda 4712\text{\AA}$ can not be described by $[\text{Ar IV}] + \text{He I}$. At the inner region of the hot wind bubble, a high excitation species additionally seems to contribute to the wind. This region was not modeled in this setup. A possible candidate might be Ne IV , although the contribution calculated by CLOUDY lies a factor of 40 below the other two lines in the main nebula.

The resulting integrated mass of the main nebula model is $0.45 M_{\odot}$. This is a high, but still feasible mass for a PN.

6.2. The shell

The sensitivity of the VLA observations, as the electron density in the shell is about two orders of magnitude below that of the main nebula, was unfortunately insufficient to obtain a direct measurement, and diagnostic diagrams using forbidden lines saturate below $n_e \approx 50 \dots 100 \text{ cm}^{-3}$. So we had to derive model calculations. Only the lines of $H\alpha$, $H\beta$, $[\text{O III}] \lambda 5007\text{\AA}$ and $[\text{N II}] \lambda 6548\text{\AA} + \lambda 6584\text{\AA}$ are sufficiently bright for the profile analysis. $[\text{O III}] \lambda 4363\text{\AA}$ was detected close to the noise level. Thus the average value of the electron temperature of $13\,200\text{K}$ (see Fig. 9) between $42''$ and $60''$ was used, instead of a free input parameter of the fit.

The CLOUDY model of the shell (Fig. 15) is using the transmitted radiation of the main nebula model. It requires a density

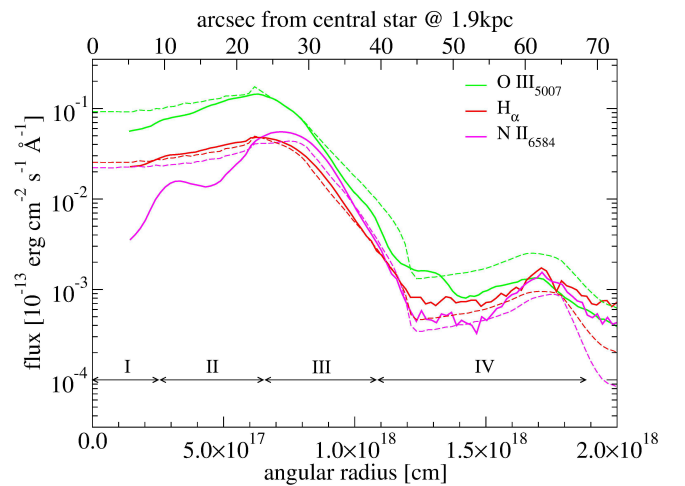


Fig. 15. The CLOUDY model of the shell (dashed lines = observations, full lines = model). As just a few lines could be used, it has the density and the filling factor as single free parameters (see text). The inner regions (I - III) are not fitted in this model, but taken from the main nebula model.

of $n_H \approx 7 \dots 30 \text{ cm}^{-3}$ (see Tab. 7). The $H\alpha / [\text{N II}]$ line ratio is slightly above unity. This ratio can be achieved only by a filling factor higher than the one in the main nebula for this plasma. The calculations provide nearly the same results for the three lines in

Table 6. The parameters of the target and of the best fit model of the main nebula (14''-38'')

at three projected radii.									
Distance: D	1.9 ± 0.2 [kpc]								
E_{B-V}	$0^m.16 \pm 0^m.01$								
Diameter: $d_{\text{mainnebula}}$	0.65 [pc]								
Mass: $M_{\text{mainnebula}}$	$0.45 M_{\odot}$								
CSPN: Rauch et al. (1999)									
T_{CSPN}	114 ± 10 [kK]								
$\log(g[\text{cgs}])$	6.62 ± 0.22								
L_{CSPN}	$570 L_{\odot}$								
M_{CSPN}	$0.56 \pm 0.01 M_{\odot}$								
$\log(n_{\text{He}}/n_{\text{H}})$	-0.56 ± 0.27								
CSPN: model									
T_{CSPN}	120 ± 2 [kK]								
L_{CSPN}	$550 \pm 15 L_{\odot}$								
projected radius	3.5×10^{17} cm	6.5×10^{17} cm	9.0×10^{17} cm						
	$\cong 13''$	$\cong 23''$	$\cong 32''$						
line (λ [Å])	obs.	model	obs.	model	obs.	model			
n_{H}		160		295		210			
$n_{\text{e}}([\text{S II}])$	180	200	350	300	200	180			
$\log(n_{\text{He}}/n_{\text{H}})$		-0.56		-1.0		-1.0			
$T_{\text{e}}(\text{phys.})$		11.7		10.2		10.6			
$T_{\text{e}}([\text{O III}])$	a) {	11.3	10.8	{	10.9	10.0	{	11.6	10.4
	b) {	10.8		{	10.5		{	11.1	
		a) calibration by Osterbrock & Ferland (2006)							
		b) calibration by Proxauf et al. (2014)							
$T_{\text{e}}([\text{N II}])$	10.5	10.1	10.0	10.0	13.3	10.3			
filling factor		0.10		0.38		0.38			

Notes. The projected radii correspond to the peaks of He II, H β and the outer edge (H α < 25% of peak). The densities are given in [cm⁻³].

Table 7. The parameters of the best fit model of the shell (38''-72'').

Parameter	
Diameter: d_{shell}	1.25 [pc]
Mass: M_{shell}	$0.5 \dots 0.8 M_{\odot}$
Filling factor	$0.5 \dots 1.0$
n_{H}	$7 \dots 30 \text{ cm}^{-3}$
$n_{\text{HII}}/n_{\text{H}}$	≥ 0.97
$T_{\text{e}}([\text{O III}])$ observed	$12.5 \dots 14.2$ [kK]
T_{e} model	13.2 [kK] (fixed)

Notes. The linear diameters correspond to the derived distance of 1.9 kpc.

the whole range: $0.5 \leq$ filling factor ≤ 1.0 . Thus we are unable to give a good conclusion about this parameter.

6.3. Comparison to the RTH models

The radiative transfer hydrodynamic (RTH) models calculated for NGC 2438 by Corradi et al. (2000), Schönberner & Steffen (2002) and Perinotto et al. (2004) lead to different results in some aspects.

The results of a 1D RTH calculation by Corradi et al. (2000) and Schönberner & Steffen (2002) show mainly recombining gas in the shell. The electron number density is one order of magnitude below that of hydrogen. In the RTH models, a temperature of 2 000 to 3 000 K is indicated. So we tested various setups with fixed electron temperatures down to 2 000 to 3 000 K, but they did not result in a fit of the ratio of the observed lines at a rea-

sonable density. Additionally, there is no detection of the [O I] lines (although those lines are affected by subtraction of the Earth's aurora). After applying estimates on the strengths and variation of the telluric lines by the methods described in Noll et al. (2012), we are quite confident about this result. The ratio predicted by the RTH models is [O I] λ 6300Å : H β = 6 : 1, but we could not confirm this result.

The resulting integrated mass of the main nebula model is $0.45 M_{\odot}$ in our calculations. It is about a factor of two above the mass calculated by Corradi et al. (2000), integrating the RTH model at their adopted distance of 1.0 kpc. At the recalculated distance of 1.9 kpc, their model gives a mass of $1.7 M_{\odot}$.

The resulting integrated mass of the shell is about 0.5 to $0.8 M_{\odot}$ in our determinations. The RTH models of Okorokov et al. (1985), Corradi et al. (2000) and Perinotto et al. (2004) assume that the shell is AGB wind material. Calculations with such an AGB wind with a terminal velocity of 10 km s^{-1} and a typical mass-loss rate of $2.5 \times 10^{-5} M_{\odot} \text{ yr}^{-1}$ result in a mass of $0.8 M_{\odot}$ in the same volume, consistent with our results. The different density used in the RTH models of Corradi et al. (2000) and Perinotto et al. (2004) leads to a very high mass estimate of $3.5 M_{\odot}$ at a distance of 1.9 kpc. This would require a very high mass loss of $\geq 1.1 \times 10^{-4} M_{\odot} \text{ yr}^{-1}$ during the late AGB phase. At the smaller distance of 1 kpc, their calculations result in an integrated mass of about $0.5 M_{\odot}$. But such small distances are excluded (see sect. 4).

The reason for the differences in the results may be found in the change of the input parameters (e.g., distance or luminosity). The RTH models used older input parameters in their calculations. Some of these parameters have changed due to new measurements and calculations. An update of the RTH models to include the new measurements would be of interest to test whether the results would converge. The evidence for clumping may also complicate the interpretation of the 1d RTH models.

7. Conclusions

The observations of NGC 2438 allow us to derive an individual distance of 1.9 ± 0.2 kpc and a foreground extinction of $E_{B-V} = 0^m.16 \pm 0^m.01$. We confirm its non-membership of the open cluster M 46, in the foreground. The large discrepancy of the nebula luminosity and the CSPN luminosity (Rauch et al. 1999) is completely resolved with these values.

The model of the main nebula indicates that the old MSPN is matter bounded. The filling factor in the inner region is lower than that in the outer part of the main nebula. This is very similar to the observational results of the spatially resolved, younger Ring and Helix nebulae. Although using only four lines in the parameter fitting, the photoionization model shows a nearly perfect representation of all observed lines. The analysis of the shock sensitive tracers indicates that shocks do not contribute to the excitation of low ionized atoms like [N II] and [S II]. This old nebula is dominated by photoionization.

The surface brightness distribution of a few bright lines by the RTH models (Corradi et al. 2000; Perinotto et al. 2004) lead to a fair representation of the whole nebula. However, the excitation and temperature throughout the nebula, and beyond, needs the handling of small scale clumps to get a self consistent model. A combination of the sophisticated hydrodynamical calculations in the RTH models, including effects of turbulence and clump formation with photoionization, would be required for a complete view.

The determined temperature of the shell and the missing bright [O I] lines lead to the conclusion that the shell

of NGC 2438 is fully ionized. Even the [O III] lines indicate a photoionized state. Final confirmation by observations of shock sensitive lines (e.g. [S II] $\lambda 6716\text{\AA}/\lambda 6732\text{\AA}$), to verify possible other excitations, is still missing. More detailed investigations to derive electron temperatures from lower ionized species (e.g., [N II] ($\lambda 6548\text{\AA} + \lambda 6584\text{\AA}$)/[N II] $\lambda 5755\text{\AA}$ or [O II] ($\lambda 3727\text{\AA} + \lambda 3729\text{\AA}$)/[O II] ($\lambda 7320\text{\AA} + \lambda 7330\text{\AA}$)), and from elements not influenced by depletion in dust grains, like [Ar III] $\lambda 5192\text{\AA}/(\lambda 7135\text{\AA} + \lambda 7751\text{\AA})$, are highly desired for the main nebula out to the shell. As recently shown by Pilyugin et al. (2010), these line ratios can achieve very high accuracies. It is also shown that the combination of those lines with H β can directly achieve abundances. Furthermore, a detailed investigation of the high excitation features in the inner hot wind bubble and of the wind itself emerging the CSPN is suggested. It is desired to complete the whole image and to give input to multi-dimensional radiative transfer hydrodynamic calculations.

Acknowledgements. We would like to thank the (anonymous) referee and the editor Malcolm Walmsley for helping to improve the manuscript. We thank Thomas Rauch (Tübingen) for extensive discussions, help with the stellar atmosphere models and providing us the ESO 3.6m (taken under proposal 64.H-0557) and SAAO 1.9m data. We thank Greg Taylor (U. of New Mexico) for providing the original FITS image of his VLA observations.

S.Ö. is supported by the Austrian *Fonds zur Wissenschaftlichen Forschung, FWF* doctoral school project W1227.

The HST Archival images were taken under Proposal 11827 (PI. Keith Noll). This research has made use of the SIMBAD and Aladin data bases, operated at CDS, Strasbourg, France.

References

- Acker, A., Marcout, J., Ochsenbein, F., Stenholm, B., Tylenda, R., Schohn, C. 1992, The Strasbourg-ESO Catalogue of Galactic Planetary Nebulae. Parts I, II (European Southern Observatory, Garching, Germany)
- Aller, L. H., & Czyzak, S. J. 1983, ApJS, 51, 211
- Armsdorfer, B., Kimeswenger, S., & Rauch, T. 2002, Revista Mexicana de A&A Conf. Series, 12, 180
- Armsdorfer, B., Kimeswenger, S., & Rauch, T. 2003, IAUS, 209, 511
- Balick, B., Gonzalez, G., Frank, A., Jacoby, G. 1992, ApJ, 392, 582
- Bensby, T., & Lundström, I. 2001, A&A, 374, 599
- Blöcker, T. 1995, A&A, 297, 727
- Chu, Y.-H., Jacoby, G.H., & Arendt, R. 1987, ApJS, 64, 529
- Colina, L., Bohlin, R.C., & Castelli, F. 1996, AJ, 112, 307
- Condon, J.J., Cotton, W.D., Greisen, E.W., Yin, Q.F., Perley, R.A., Taylor, G.B., & Broderick, J.J. 1998, AJ, 115, 1693
- Copetti, M.V.F., & Writzl, B.C. 2002, A&A, 382, 282 (2002)
- Corradi, R. L. M., Schönberner, D., Steffen, M., & Perinotto, M. 2000, A&A, 354, 1071
- Corradi, R. L. M., Schönberner, D., Steffen, M., & Perinotto, M. 2003, MNRAS, 340, 417
- Dalnodar, S., & Kimeswenger, S. 2011, Asymmetric Planetary Nebulae 5 Conference, 81P
- Decin, L., 2012, AdSpR, 50,843
- Fluks, M., & The, P. 1992, A&A, 255, 477
- Ferland, G.J., Korista, K.T., Verner, D.A., Ferguson, J.W., Kingdon, J.B., & Verner, E.M. 1998, PASP, 110, 761
- Ferland, G. J., Porter, R. L., van Hoof, P. A. M. 2013, Rev. Mex. A&A, 49, 137
- Guerrero, M. A., & Machado, A. 1999, ApJ, 522, 378
- Guerrero, M. A., Toalá, J. A., Medina, J. J., Luridiana, V., Miranda, L. F., Riera, A., & Velázquez, P. F. 2013, A&A, 557, A121
- Kaler, J. B. 1983, ApJ, 271, 188
- Kaler, J. B., Shaw, R. A., & Kwitter, K. B. 1990, ApJ, 359, 392
- Keenan, F.P., Kingston, A.E., Johnson, C.T. 1988, A&A, 202, 253
- Khromov, G. S. 1989, Space Sci. Rev., 51, 339
- Kingsburgh, R. L., & Barlow, M. J. 1994, MNRAS, 271, 257
- García Lario, P., Machado, A., Riera, A., Mampaso, A., & Pottasch, S. R. 1991, A&A, 249, 223
- Kiss, L. L., Szabó, Gy. M., Balog, Z., Parker, Q. A., & Frew, D. J. 2008, MNRAS, 391, 399
- Magrini, L., Perinotto, M., Corradi, R. L. M., & Mampaso, A. 2003, A&A, 400, 511
- Majaess, D., Turner, D., & Lane, D. 2007, PASP, 119,1349
- Matsuura, M., Speck, A. K., McHunu, B. M., et al. 2009, ApJ, 700, 1067
- Meatheringham, S.J., Wood, P.R., & Faulkner, D.J. 1988, ApJ, 334, 862
- Mikołajewska, J., Brandi, E., Hack, W., Whitelock, P. A., Barba, R., Garcia, L., Marang, F. 1999, MNRAS, 305, 190
- Noll, S., Kausch, W., Barden, M., Jones, A. M., Szyszka, C., Kimeswenger, S., & Vinther, J. 2012, A&A, 543, A92
- O'Dell, C. R., Balick, B., Hajian, A. R., Henney, W. J., Burkert, A. 2003, Rev. Mex. A&A Ser. Conf., 15, 29
- O'Dell, C. R., Henney, W. J., Ferland, G. J. 2005, AJ, 130, 172
- Okorokov, V. A., Shustov, B. M., Tutukov, A. V., & Yorke, H. W. 1985, A&A, 142, 441
- Osterbrock, D. E., & Ferland, G. J. 2006, Astrophysics of gaseous Nebulae and active Galactic Nuclei (University Science Books, Sausalito, CA)
- Paunzen, E., Heiter, U., Netopil, M., & Soubiran, C. 2010, A&A, 517, A32
- Perinotto, M., Schönberner, D., Steffen, M., & Calonaci, C. 2004, A&A, 414, 993
- Phillips, J. P. 2004, RMxAA, 40, 193
- Pilyugin, L.S., Vílchez, J.M., & Thuan, T.X. 2010, ApJ, 720, 1738
- Proxau, B., Öttl, S., & Kimeswenger, S. 2014, A&A, 561, A10
- Ramos-Larios, G., Vázquez, R., Guerrero, M. A., Olgúin, L., Marquez-Lugo, R. A., & Bravo-Alfaro, H. 2012a, MNRAS, 423, 3753
- Ramos-Larios, G., Guerrero, M. A., Vázquez, R., & Phillips, J. P. 2012b, MNRAS, 420, 1977
- Ramos-Larios, G., & Phillips, J. P. 2012, MNRAS, 425, 1091
- Rauch, T., Köppen, J., Napiwotzki, R., & Werner, K. 1999, A&A, 347, 169
- Rauch, T. 2003, IAUS, 209, 191
- Reid, W. A., & Parker, Q. A. 2010, PASA, 27, 187
- Ringat, E. 2012, ASP Conference Series, 452, 99
- Schmeja, S., & Kimeswenger, S. 2001, A&A, 377, L18
- Schneider, S. E., & Buckley, D. 1996, ApJ, 459, 606
- Schönberner, D. & Steffen, M. 2002, RMxAC, 12, 144
- Sharma, S., Pandey, A. K., Ogura, K., Mito, H., Tarusawa, K., & Sagar, R. 2006, AJ, 132, 1669
- Speck, A. K., Meixner, M., Jacoby, G. H., Knezek, P. M. 2003, PASP, 115, 170
- Stanghellini, L., & Kaler, J.B. 1989, ApJ, 343, 811
- Taylor, G. B., & Morris, A. 1993, ApJ, 409, 720
- Torres-Peimbert, S., & Peimbert, M. 1977, Rev.Mex.A&A., 2, 181
- van de Steene, G. C., & Zijlstra, A. A. 1995, A&A, 293, 541
- Vicini, B., Natta, A., Marconi, A., Testi, L., Hollenbach, D., & Draine, B. T. 1999, A&A, 342, 823
- Vollmer, B., Gassmann, B., Derrière, S., Boch, T., Louys, M., Bonnarel, F., Dubois, P., Genova, F., & Ochsenbein, F. 2010, A&A, 511, A53
- Warmels, R.H. 1991, PASP Conf. Series, 25, 115
- Zhang, Y., Hsia, C.-H., & Kwok, S. 2012, ApJ, 755, 53
- Zijlstra, A.A., Pottasch, S.R., & Bignell, C. 1989, A&AS, 79, 329

Appendix A: The model results of the main nebula

The table gives the full model of the best fit. The normalization on the left hand side is relative to $H\beta$ at each column individually. This allows the view on line ratios as they are commonly used in nebular spectroscopy. The right hand table is normalized to $H\beta$ only in the middle column, to give a better view on the radial evolution of individual line fluxes.

Table A.1. The measured line intensities vs. the model lines of the best fit model of the main nebula.

line (λ [Å])	$3.5 \times 10^{17} \text{cm} \equiv 13''$		$6.5 \times 10^{17} \text{cm} \equiv 23''$		$9.0 \times 10^{17} \text{cm} \equiv 32''$		line (λ [Å])	$3.5 \times 10^{17} \text{cm} \equiv 13''$		$6.5 \times 10^{17} \text{cm} \equiv 23''$		$9.0 \times 10^{17} \text{cm} \equiv 32''$	
	obs.	model	obs.	model	obs.	model		obs.	model	obs.	model	obs.	model
$H\theta$ (3798)	6.7	{5.57	7.0	{5.35	6.2	{5.3	$H\theta$ (3798)	4.5	{3.63	6.9	{5.35	2.9	{2.4
$He\ II$ (3797)		{0.11		{0.04		{—	$He\ II$ (3797)		{0.07		{0.04		{—
$H\eta$ (3835)	9.6	7.7	9.7	7.4	7.2	7.3	$H\eta$ (3835)	6.4	5.0	9.5	7.4	3.4	3.3
$Ne\ III$ (3869)	122	140	140	116	170	138	$Ne\ III$ (3869)	82	91	140	116	80	62
$H\zeta$ (3889)		{10.9		{10.5		{10.4	$H\zeta$ (3889)		{7.1		{10.5		{4.7
$He\ I$ (3889)	22	{10.4	23	{9.7	30	{10.9	$He\ I$ (3889)	15	{6.8	23	{9.7	14	{4.9
$H\epsilon$ (3970)		{16.3		{15.9		{16.0	$H\epsilon$ (3970)		{10.6		{15.9		{7.2
$Ne\ III$ (3968)	52	{42.2	62	{35.0	68	{41.8	$Ne\ III$ (3968)	35	{27.5	61	{35.0	32	{18.8
$He\ I$ (4026)	2.5	2.21	2.1	2.11	3.4	2.36	$He\ I$ (4026)	1.7	1.44	2.1	2.11	1.6	1.06
[S II] (4070)	2.4	3.76	3.9	3.98	8.3	5.62	[S II] (4070)	1.6	2.45	3.8	3.98	3.9	2.53
$H\delta$ (4102)	27	26.4	26	25.9	26	26.0	$H\delta$ (4102)	18	17.2	25	25.9	12	11.7
$He\ II$ (4200)	0.7	0.69	0.6	0.27			$He\ II$ (4200)	0.5	0.45	0.6	0.27		
$C\ II$ (4267)	1.8	0.66	1.0	0.69	0.9	0.67	$C\ II$ (4267)	1.2	0.43	1.0	0.69	0.4	0.30
$H\gamma$ (4340)	49	47.2	51	46.8	51	46.9	$H\gamma$ (4340)	33	30.8	50	46.8	24	21.1
[O III] (4363)	10	9.77	10	6.13	8	6.56	[O III] (4363)	6.7	6.37	9.8	6.13	3.7	2.95
$He\ I$ (4471)	4.6	4.62	4.0	4.39	6.8	4.93	$He\ I$ (4471)	3.1	3.01	3.9	4.39	3.2	2.22
$He\ II$ (4542)	1.8	1.32	0.9	0.49			$He\ II$ (4542)	1.2	0.86	0.9	0.49		
$He\ II$ (4686)	49	39.6	30	31.5	5	2.5	$He\ II$ (4686)	33	25.8	29	31.5	2.3	1.14
$He\ I$ (4713)		{0.49		{0.45		{0.64	$He\ I$ (4713)		{0.32		{0.45		{0.64
$Ar\ IV$ (4711)	3.0	{2.85	1.5	{0.64	—	—	$Ar\ IV$ (4711)	2.0	{1.86	1.44	{0.64	—	—
$Ne\ IV$ (4714)							{0.08						
$Ar\ IV$ (4740)	1.6	2.18	0.6	0.49				$Ar\ IV$ (4740)	1.1	1.42	0.6	0.49	
$H\beta$ (4961)	100	100	100	100	100	100	$H\beta$ (4961)	67	65.2	98	100	47	45
$He\ I$ (4922)	1.1	1.27	1.1	1.22	1.4	1.36	$He\ I$ (4922)	0.75	0.83	1.1	1.22	0.66	0.61
[O III] (4959)	325	363	327	310	240	293	[O III] (4959)	218	237	320	310	113	132
[O III] (5007)	979	1097	982	935	723	882	[O III] (5007)	656	715	962	935	340	397
$N\ I$ (5199)	1.6	0.81	2.8	0.84	13.2	2.02	$N\ I$ (5199)	1.1	0.53	2.7	0.84	6.2	0.91
$Ne\ II$ (5412)	4.0	3.02	2.6	1.16			$Ne\ II$ (5412)	2.7	1.97	2.5	1.16		
$Cl\ III$ (5518)			1.6	1.15			$Cl\ III$ (5518)			1.6	1.15		
$Cl\ III$ (5538)			0.8	0.86			$Cl\ III$ (5538)			0.8	0.86		
[N II] (5755)	2.8	3.48	3.9	3.63	11.9	6.93	[N II] (5755)	1.9	2.27	3.9	3.63	5.6	3.12
$He\ I$ (5876)	13	13.42	13	12.95	23	13.64	$He\ I$ (5876)	9.0	8.75	12.6	12.95	11.2	6.14
[N II] (6548)	64	81	93	87	170	151	[N II] (6548)	43	53	91	87	80	68
$H\alpha$ (6563)	293	290	294	291	291	291	$H\alpha$ (6563)	203	189	290	291	137	131
[N II] (6584)	178	239	279	256	434	449	[N II] (6584)	119	156	274	256	204	202
$He\ I$ (6678)	2.4	3.80	4.3	3.67	5.7	4.04	$He\ I$ (6678)	1.6	2.48	4.2	3.67	2.7	1.82
[S II] (6716)	19	29.3	37	31.44	74	50.0	[S II] (6716)	13	19.1	36	31.4	35	22.4
[S II] (6731)	15	26.1	31	28.2	66	40.0	[S II] (6731)	10	17.0	30	28.2	31	17.9
$He\ I$ (7065)	3.4	2.62	2.7	2.46	1.7	2.67	$He\ I$ (7065)	2.3	1.71	2.6	2.46	0.8	1.20
$Ar\ III$ (7135)	22	25.9	25	27.2	23	31.5	$Ar\ III$ (7135)	15	16.9	25	27.2	11	14.2

Notes. Radii correspond to those described in Tab. 6. The four lines used for the fitting procedure of the free parameters are underlined. The lines are normalized to $H\beta = 100$ at each column individually in the left part of the table (marked in bold face). The right hand part gives the fluxes relative to the brightest point in $H\beta = 100$ ($\equiv 2 \times 10^{-13} \text{ ergs cm}^{-1} \text{ s}^{-1} \text{ \AA}^{-1}$ per slit). The regions are selected as 'inner edge', ' $H\alpha$ peak' and 'outer edge'. Each of them is a narrow screenshot of only $2''$.